ACS Catalysis
RESEARCH ARTICLE
pubs.acs.org/acscatalysis

Ir_6 Clusters Compartmentalized in the Supercages of Zeolite NaY: Direct Imaging of a Catalyst with Aberration-Corrected Scanning Transmission Electron Microscopy

Ceren Aydin,[†] Jing Lu,[†] Masayuki Shirai,[‡] Nigel D. Browning,[†,§] and Bruce C. Gates[*,†]

[†]Department of Chemical Engineering and Materials Science, University of California Davis, One Shields Avenue, Davis, California 95616, United States

[‡]Research Center for Compact Chemical Systems, National Institute of Advanced Industrial Science and Technology (AIST), 4-2-1 Nigatake, Miyagino, Sendai 983-8551, Japan

[§]Physical and Life Sciences Directorate, Lawrence Livermore National Laboratory, 700 East Avenue, Livermore, California 94550, United States

S *Supporting Information*

ABSTRACT: By use of the precursor $Ir(CO)_2(acac)$ (acac is acetylacetonate), a ship-in-a-bottle synthesis was used to prepare $Ir_6(CO)_{16}$ and, by decarbonylation, clusters well approximated as Ir_6 in the supercages of zeolite NaY. The samples were characterized by infrared and extended X-ray absorption fine structure (EXAFS) spectroscopies and imaged by aberration-corrected scanning transmission electron microscopy with a high-dose electron beam ($\sim 10^8$ $e^-/Å^2$, 200 kV), and the catalyst performance was characterized by turnover frequencies for ethene hydrogenation at 298 K and atmospheric pressure. The images characterizing a sample with about 17% of the supercages occupied by decarbonylated nanoclusters indicated clusters well approximated as Ir_6, with diameters consistent with such clusters, and some of the images show the clusters with atomic resolution and indicating each of the 6 Ir atoms. The cluster size was confirmed by EXAFS spectra. Two bonding positions of the Ir_6 clusters in the supercages were distinguished; 25% of the clusters were present at T5 sites and 75% at T6 sites. The results represent the first example of the application of high-dose electron beam conditions to image metal nanoclusters in a nanoporous material; the data are characterized by a high signal-to-noise ratio, and their interpretation does not require any image processing or simulations. These statements are based on images determined in the first 5 s of exposure of the catalyst to the electron beam; thereafter, the electron beam caused measurable deterioration of the zeolite framework and thereupon aggregation of the iridium clusters.

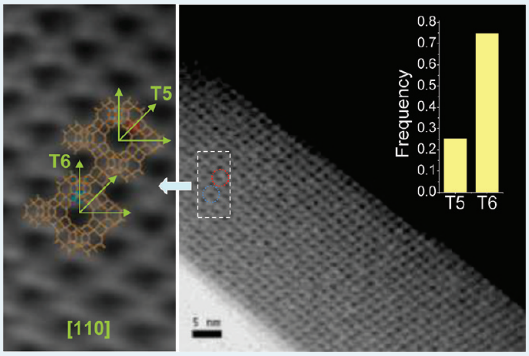

KEYWORDS: hexairidium clusters, zeolite NaY, aberration-corrected scanning transmission electron microscopy, zeolite-encaged nanoclusters

INTRODUCTION

Many practical catalysts consist of nanostructures dispersed on the internal surfaces of porous solids. These materials are typically highly nonuniform, consisting of nanoparticles of various sizes and shapes on supports having surfaces that are nonuniform in composition and structure.[1] When the catalytic nanostructures are less than roughly 1 nm in diameter, their properties become substantially different from those of the bulk material, and the catalytic properties are size-dependent even for reactions classed as structure insensitive.[2] To gain fundamental understanding of the smallest supported catalytic species, it is helpful to synthesize them with a high degree of structural uniformity. Our goal was to prepare and characterize uniform metal nanoclusters, using a faujasite zeolite as the support, chosen because its crystalline porous structure offers the opportunity to encapsulate the nanoclusters in uniform cages with diameters of about 1 nm.[3]

Investigations of metal clusters supported on metal oxides and zeolites include many formed from treatments of supported organometallic precursors.[4−6] Most of the characterizations of such nanoclusters have been done spectroscopically, and there is a lack of direct evidence of size distributions and locations of the nanoclusters in the pores. But recent advances in high-angle annular dark-field (HAADF) aberration-corrected scanning transmission electron microscopy (STEM) have markedly facilitated the collection of such information.[7−10]

In the STEM mode of imaging, there is a trade-off between the high resolution provided by a highly focused probe on the one hand and sample deterioration caused by the high-energy electron

Received: August 4, 2011
Revised: September 30, 2011
Published: October 03, 2011

ACS Publications © 2011 American Chemical Society

beam, on the other hand. The electron beam causes destruction of zeolite frameworks and migration of the metal species—these processes typically occur within seconds. To minimize these effects, low-dose imaging was used to provide the first STEM images of isolated metal clusters in the framework of a highly dealuminated zeolite, ultrastable HY,[11] but the data[11] are characterized by substantial noise, requiring extensive image processing to provide useful structural information.

Now, by recording STEM images quickly enough to essentially avoid sample degradation by the electron beam, we have used a high-dose electron beam ($\sim 10^8$ $e^-/Å^2$, 200 kV) to investigate nearly uniform iridium clusters in the pores of a zeolite without compromising the signal-to-noise ratio in the images.

SYNTHESIS OF ZEOLITE-SUPPORTED Ir_6 CLUSTERS

Samples consisting of zeolite-supported mononuclear iridium complexes were synthesized by the reaction of $Ir(CO)_2(acac)$ (acac is acetylacetonate) with zeolite NaY, as described elsewhere.[12] This zeolite was chosen because it has a high degree of crystallinity and facilitates the synthesis of iridium carbonyl clusters by a ship-in-a-bottle method.[13,14] In the first step of cluster formation, the powder sample incorporating the mononuclear iridium complexes was carbonylated by treatment with flowing CO at 448 K and atmospheric pressure for 16 h. This treatment was followed by decarbonylation of the iridium cluster carbonyls in flowing helium at 573 K at atmospheric pressure for 6 h.

Considering the fact that the supercages of zeolite NaY are 1.3 nm in diameter and the apertures connecting these cages are 0.74 nm in diameter,[15] the growth of iridium carbonyl clusters under our treatment conditions was expected to be limited by the supercage dimensions.[16] Hexairidium hexadecacarbonyl, $Ir_6(CO)_{16}$, is approximately 1.1 nm in diameter, as shown by the reported crystallographic data.[17] On the basis of these values, we expected $Ir_6(CO)_{16}$ to be the largest of the known molecular iridium carbonyl clusters to fit in a faujasite supercage and at the same time be too large to diffuse through the apertures (Figure 1)—thus, it was expected that these clusters could be entrapped in the supercages,[18] leading to site isolation and uniformity.

Recognizing that only one hexairidium cluster fits in a supercage and assuming that all the iridium in each sample was present in these cages in the form of Ir_6, we calculated the occupancy of the supercages for various iridium loadings. Filling all of the supercages in zeolite NaY with Ir_6 would require an iridium loading of 31 wt %.

To determine how STEM could be used effectively to characterize such samples and to provide a contrast with a sample containing too much iridium to be present only in supercages, we prepared two samples, one with slightly more than 31 wt % iridium loading and one with a markedly lower loading of 10 wt % iridium. The two-stage cluster formation treatment described above was applied to each sample.

The sample with the higher iridium loading was expected to have some iridium outside of the zeolite pores (the Ir_6/supercage ratio was 1.2, presuming all the iridium had been present in hexairidium clusters). HAADF-STEM images of this sample (Figure 2) clearly demonstrate the presence of clusters/particles larger than Ir_6 (which has a diameter of approximately 0.6 nm, as calculated from the crystallographic data reported for $Ir_6(CO)_{16}$[17]). The iridium nanoparticles in this highly loaded sample are nonuniform, more or less as in a conventional supported metal catalyst. This sample was clearly not of primary interest in this research.

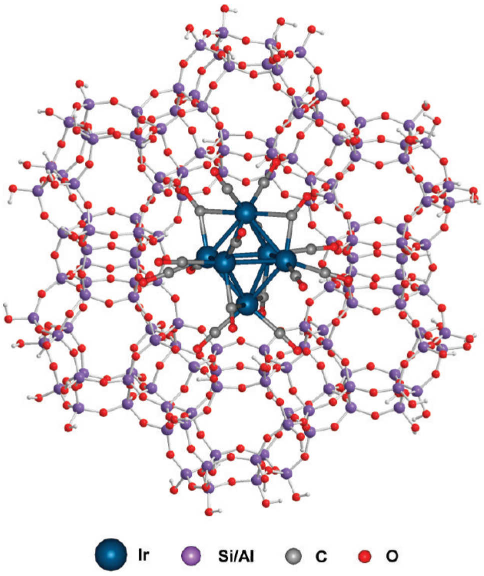

Figure 1. Schematic representation of $Ir_6(CO)_{16}$ encapsulated in a supercage of zeolite NaY (a faujasite).

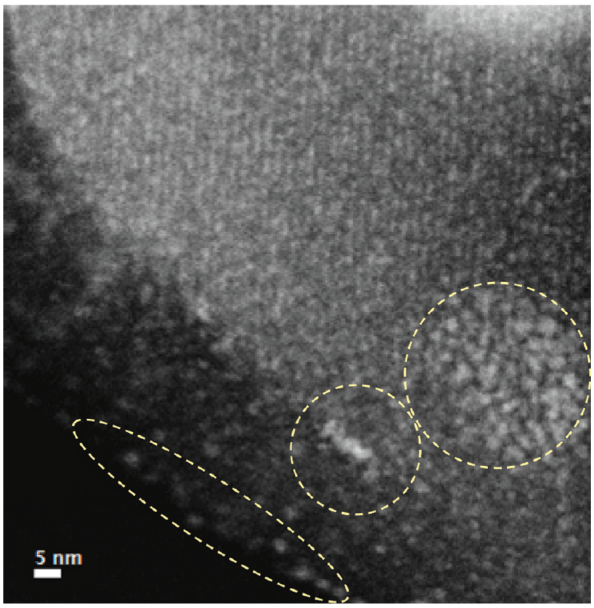

Figure 2. HAADF-STEM image of sample containing 33 wt % Ir: the image clearly demonstrates the presence of nonuniform iridium clusters/particles on the outer surface of the zeolite (see encircled areas; the clusters and particles larger than Ir_6 are indicated by the bright features that are nonuniform in size and shape). The orientation of this zeolite crystal was not optimal for observation of the iridium clusters inside the zeolite pores.

Of more importance for our goals was the sample containing 10 wt % iridium, which was calculated to have a 17% occupancy of the supercages, provided that all the iridium was in the form of Ir_6 clusters and present in the supercages. The HAADF-STEM images of this sample (Figures 3 and 4A) indicate iridium clusters within the zeolite pore structure and give no evidence of iridium outside the zeolite framework. Thus, this sample provided the opportunity for a detailed investigation of the nanoclusters in the zeolite; it was characterized spectroscopically as well as by STEM.

Table 1. Structural Parameters Corresponding to the Fit Models for EXAFS Data Characterizing Species Formed by Treatment of Zeolite NaY-Supported $Ir(CO)_2(acac)$[a]

	EXAFS Results					
treatment conditions	shell	N	R (Å)	$10^3 \times \Delta\sigma^2$ (Å^2)	ΔE_0 (eV)	supported species modeled as
10% CO in helium at 448 K for 16 h	$Ir-O_{zeolite}$	0.8	2.11	1.2	8.0	$Ir_6(CO)_{16}$/zeolite NaY
	$Ir-C_{CO}$	2.2	1.93	6.5	−4.2	
	$Ir-O_{CO}$	2.2	3.00	2.8	−7.6	
	$Ir-Ir_{first}$	4.0	2.74	5.2	−8.0	
	$Ir-Ir_{second}$	0.9	3.90	3.6	−8.0	
	Ir−Al	*b*	*b*	*b*	*b*	
10% CO in helium at 448 K for 16 h, followed by decarbonylation in helium at 573 K for 6 h	$Ir-O_{zeolite}$	1.3	2.09	9.3	−5.6	Ir_6/zeolite NaY
	$Ir-C_{CO}$	*b*	*b*	*b*	*b*	
	$Ir-O_{CO}$	*b*	*b*	*b*	*b*	
	$Ir-Ir_{first}$	3.9	2.64	7.6	−1.6	
	$Ir-Ir_{second}$	0.9	3.74	4.8	12.0	
	Ir−Al	0.8	3.41	1.1	5.1	

[a] Notation: N, coordination number; R, distance between absorber and backscatterer atoms; $\Delta\sigma^2$, variance in the absorber-backscatterer distance; ΔE_0, inner potential correction. Error bounds (accuracies) characterizing the structural parameters are estimated to be as follows: N, ± 20%; R, ± 0.02 Å; $\Delta\sigma^2$, ± 20%; and ΔE_0, ± 20%. [b] Contribution not detectable. Details of the EXAFS fitting are provided in the Supporting Information.

CHARACTERIZATION OF SAMPLE CONSISTING OF SUPPORTED IRIDIUM NANOCLUSTERS BY INFRARED AND X-RAY ABSORPTION SPECTROSCOPIES

Infrared (IR) and extended X-ray absorption fine structure (EXAFS) spectra were obtained to characterize the samples both following the carbonylation step and following the decarbonylation steps described above. The IR spectra of the carbonylated sample (Supporting Information, Figure SI-1a) indicate a mixture of the two $Ir_6(CO)_{16}$ isomers, that with face-bridging and that with edge-bridging ligands (see Supporting Information for a detailed interpretation of the IR spectra).[17,19,20] In contrast, the IR spectra characterizing the sample after decarbonylation (Supporting Information, Figure SI-1b) lack detectable bands in the ν_{CO} region, indicating that the decarbonylation was essentially complete.

As summarized in Table 1, the EXAFS data (see details of EXAFS fitting in Table SI-1 in Supporting Information) show that the sample after the carbonylation step can be well represented as hexairidium carbonyl clusters, $Ir_6(CO)_{16}$, grown in the supercages of the zeolite. First- and second-shell Ir−Ir contributions were found with coordination numbers approximately equal to 4 and 1, respectively (Table 1), as expected for hexairidium clusters with octahedral frames, as in $Ir_6(CO)_{16}$.[17] The Ir−Ir distances were found to be 2.74 and 3.90 Å for the first- and second-shell contributions, respectively, matching the crystallographic data representing $Ir_6(CO)_{16}$.[17] As a result of carbonylation, $Ir-C_{CO}$ or $Ir-O_{CO}$ contributions (where the subscripts denote carbonyl ligands), were also detected in EXAFS spectra after this treatment step. On the other hand, the EXAFS data characterizing the sample after decarbonylation gave no evidence of $Ir-C_{CO}$ or $Ir-O_{CO}$ contributions, consistent with the IR data. The first- and second-shell Ir−Ir coordination numbers remained constant after decarbonylation, indicating the intact hexairidium cluster framework after decarbonylation. The Ir−Ir distances characterizing the decarbonylated species were found to be 2.64 and 3.74 Å, respectively, indicating a shrinkage of the Ir_6 framework as a result of the decarbonylation (but the change is too small to distinguish by STEM). Estimates of the sizes of the $Ir_6(CO)_{16}$ clusters and decarbonylated Ir_6 clusters based on the EXAFS data were determined from the Ir−Ir and Ir−O distances and the atomic radii of iridium and oxygen to be 1.2 and 0.64 nm, respectively.

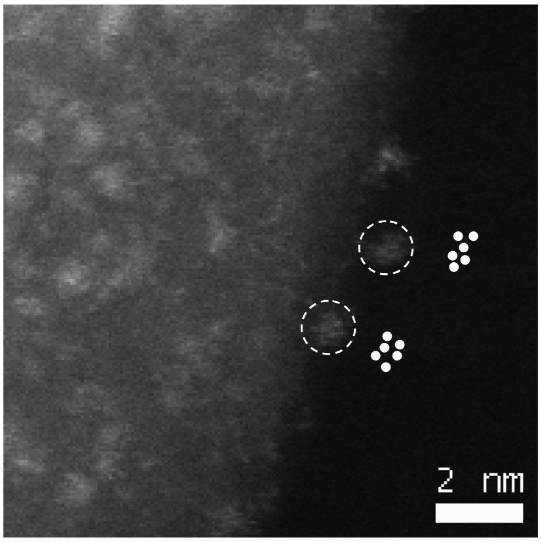

Figure 3. Aberration-corrected HAADF-STEM image of zeolite NaY-supported sample containing 10 wt % iridium after decarbonylation of the clusters: image showing Ir_6 clusters with atomic resolution. Superimposed on the image next to two clusters are models of the cluster structures indicating the metal frameworks, which, because of electron-beam damage, are no longer octahedral, as they were in $Ir_6(CO)_{16}$.

In summary, the EXAFS and IR data characterizing the sample containing 10 wt % Ir demonstrate the formation of $Ir_6(CO)_{16}$ supported on zeolite NaY after the first step of treatment with CO and the conversion of these iridium carbonyl clusters, on average, into decarbonylated hexairidium clusters by treatment in helium. These results are in good agreement with previous observations.[21]

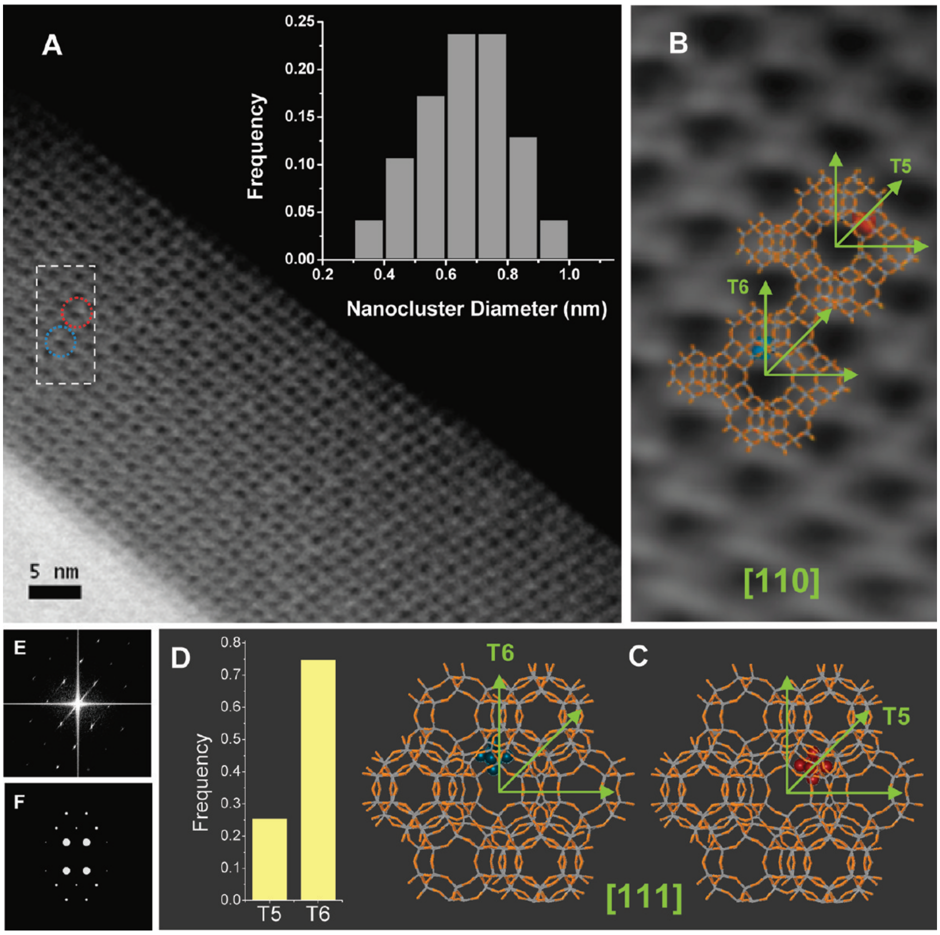

Figure 4. **(A)** Unprocessed aberration-corrected HAADF-STEM image of zeolite NaY-supported sample containing 10 wt % iridium after decarbonylation of clusters, showing the zeolite framework in the [110] direction, and a histogram showing the distribution of the nanocluster diameters; the images indicate Ir_6 clusters compartmentalized in the supercages of the zeolite. **(B)** A magnified view of the dashed-rectangular area in (A) containing the two Ir_6 clusters encircled. A cluster at a T5 site is represented in red, and a cluster at a T6 site is represented in blue. Simulations of the faujasite in the [110] projection are superimposed on the experimental image indicating Ir_6 clusters. The arrows indicate the relative orientations of the T5 and T6 sites with respect to the [110] direction of the zeolite crystal. **(C)** Simulated faujasite models in the [111] projection corresponding to the location of the two Ir_6 clusters shown in (B). **(D)** Frequencies of Ir_6 clusters located in T5 and T6 sites. **(E)** Fast Fourier transform of the experimental image shown in (A). **(F)** Theoretical diffraction pattern of zeolite NaY in the [110] direction.

STEM EVIDENCE OF ZEOLITE-ENCAGED Ir_6 CLUSTERS

High-dose aberration-corrected HAADF-STEM imaging was used to characterize the sample containing 10 wt % iridium and incorporating the decarbonylated iridium clusters. In the images, there is a strong contrast between the heavy Ir atoms (atomic number $Z = 77$) and the zeolite, which consists of light atoms, Al (Z = 13), Si (Z = 14), and O (Z = 8) along with the zeolite exchange cation Na^+ (Z = 11). Because the intensity of the dominant scattering mechanism that gives rise to the contrast in HAADF-STEM images is proportional to Z^2, it is more straightforward to interpret these images than the conventional TEM images of such supported clusters as reported previously[22]—in the earlier work, the clusters could not be distinguished from the support in the images.

The aberration-corrected HAADF-STEM image of the sample containing 10 wt % Ir (Figure 3) shows—with atomic resolution—the clusters formed after the two-step treatment involving carbonylation and decarbonylation steps. The image at a high magnification clearly shows the presence of clusters incorporating 6 Ir atoms each. The image (Figure 3) shows that the metal frames were no longer octahedral (as in the precursor $Ir_6(CO)_{16}$ and as in the initially formed Ir_6, as indicated by the EXAFS spectra (Table 1)). We infer that the structure changed slightly under the influence of the electron beam (more comments about the effects of the electron beam are presented below).

The orientation of the zeolite crystallite shown in the image of Figure 3 was not optimal for analysis of the locations of clusters within the supercages of the zeolite. Consequently, we show another HAADF-STEM image of the sample containing 10 wt % Ir (Figure 4A), again recorded under high-dose imaging conditions. This image is characterized by a high signal-to-noise ratio, enabling us to make direct observations of the locations of the iridium nanoclusters in the zeolite pores without the need for image processing. The fast Fourier transform of the experimental image shown in Figure 4E matches precisely the simulated diffraction pattern characterizing the [110] orientation of the faujasite shown in Figure 4F, indicating that the zeolite crystallite was imaged in this orientation—which is the optimal orientation for a thorough analysis of the sizes and locations of the clusters in the zeolite framework. This orientation of the crystallite is clearly the best for examination of the cluster locations because it provides crystallographic projections with minimal overlap of Ir atoms by zeolite framework atoms.[11]

To characterize the nanoclusters in this sample, STEM was used to determine the distribution of nanocluster diameters by analysis of the intensity profiles drawn across clusters in the STEM image. The profiles were fitted to a Gaussian distribution function, and full-width-at-half-maximum values were determined as measures of the diameters of the individual clusters (see Experimental Methods for details of cluster diameter measurements).

As depicted in the histogram of Figure 4A, the clusters formed in the sample containing 10 wt % iridium were nearly monodisperse—the mean cluster diameter was found to be 0.68 ± 0.14 nm, where the error bound represents the standard deviation determined in the analysis for a population of 85 clusters in the STEM image; the histogram indicates a narrow and nearly Gaussian distribution of cluster diameters that is consistent with a unimodal distribution of clusters in the zeolite.[23,24] The fact that there is a distribution of measured cluster diameters is explained by standard blurring effects in STEM images (associated with electron beam probe size, vibrational instabilities, irradiation effects, off-focus, beam broadening, etc). These effects are expected to cause a slight overestimation of the cluster diameters in addition to a broadening of the size distribution.[25] Moreover, the octahedral frame of Ir_6 might be characterized by different apparent diameters, depending on the projection of the cluster in the image and how it is anchored to the zeolite. These variations could also influence the cluster size distribution. Furthermore, the electron beam may have affected the structure of the Ir_6 framework, as indicated in Figure 3. These points help to explain the difference between the average cluster diameter determined by STEM (0.68 nm), the crystallographic diameter of the hexairidium frame in $Ir_6(CO)_{16}$ (0.6 nm),[17] and the diameter of the decarbonylated Ir_6 cluster calculated from the EXAFS data (0.64 nm).[26] In summary, we infer that the images are consistent with the presence of predominantly Ir_6 clusters in the zeolite.

These results agree well with the report by Tesche et al.[22] characterizing hexairidium clusters in zeolite NaY, although his results were limited because the iridium clusters could hardly be distinguished in his images—because the imaging mode was conventional TEM, and the interpretation of the contrast in the images was not straightforward, and it was not possible to resolve the effects of overlapped mass−thickness and diffraction contrast of the sample.

HAADF-STEM almost eliminates the phase and diffraction contrast from the crystalline support and the metal species, and distinguishing the metal species from the support becomes easier, especially when the intensity depends primarily on the atomic number difference (*Z*-contrast) of the elements in the structure of supported metal catalysts. Therefore, this mode of imaging is excellently suited to samples such as ours incorporating a heavy metal (iridium) and a support consisting of light elements (zeolite NaY).

An essential point is that the STEM analysis is consistent with the spectroscopic data and earlier results and thereby provides the basis for a much more detailed analysis of the zeolite-supported metal nanoclusters than has heretofore been available. The images give no evidence of clusters outside of the supercages, consistent with the results showing that the average diameter of the decarbonylated clusters is 0.68 ± 0.14 nm (markedly less than the zeolite supercage diameter is 1.3 nm) and consistent with the synthesis conditions giving a cluster loading enough to fill only 17% of the supercages.

■ LOCATIONS OF Ir_6 CLUSTERS IN THE ZEOLITE SUPERCAGES

In addition to evidence of the size distribution and uniformity of the encaged clusters, the STEM images show where the clusters are anchored in the zeolite cages. Aberration-corrected HAADF-STEM imaging is unique in its ability to locate nanoclusters in such samples; it requires high signal-to-noise ratios in the images, as we have obtained.

With the zeolite imaged in the [110] orientation, as in our case, the resultant pattern consists of an array of cavities whereby two apertures on opposite sides of a supercage overlap, corresponding to the open spaces appearing in an array, as shown in the images of Figure 4A and Figure 4B. Thus, the images allow us to locate the nanoclusters in individual supercages. The results show that two distinct bonding positions for the clusters in the supercages[11] can be observed directly.

As shown in Figure 4, with the center of the array of cavities assigned as the origin, the images show that the iridium clusters at the horizontal and the vertical positions indicate clusters bonded at T5 sites and the ones on the diagonal position clusters bonded at T6 sites.[11] The circled bright features in Figure 4A are examples of each of the iridium clusters located in these two sites (T5 in red circle and T6 in blue circle), and a magnified image of that section is shown in Figure 4B, where the circled clusters in T5 and T6 sites are highlighted in red and blue, respectively.

We analyzed all the parts of the image providing the locations of clusters, finding that the ratio of Ir_6 clusters in T6 sites to Ir_6 clusters in T5 sites was approximately 3; this conclusion is based on an analysis including a population of 85 clusters, with the frequencies represented in Figure 4D. This result is in agreement with the reported analysis[11] carried out for similar iridium clusters in dealuminated HY zeolite, formed by reduction of initially supported $Ir(C_2H_4)_2$ species by H_2. Because the previous investigation required extensive image processing and simulation, it was far more time-consuming than ours and more susceptible to artifacts.

To our knowledge, the investigation presented here is the first example of such a precise and direct determination of the locations of nanoclusters in a porous solid incorporating crystallographically defined cages. The results demonstrate the power of aberration-corrected HAADF-STEM imaging to provide high-quality images of nanoclusters even in the pores of a material that is prone to beam damage—and no imaging processing or simulation was needed.

■ STABILITY OF Ir_6 CLUSTERS IN ZEOLITE NaY UNDER THE INFLUENCE OF THE ELECTRON BEAM, EVIDENCE OF CLUSTER STABILIZATION BY THE SUPERCAGES

To test the stability of the supported clusters in the electron beam, we recorded consecutive images in the same region of the sample for a period of 20 s. As shown in Figure 5, the zeolite framework, which was imaged in the [111] orientation (evidenced by the experimental diffraction pattern), began to deteriorate during exposure to the beam, with the crystalline structure starting to disappear, as shown by the changes in the fast Fourier transforms of the images. The images show that in this time frame the zeolite framework was only partially destroyed and that there was no

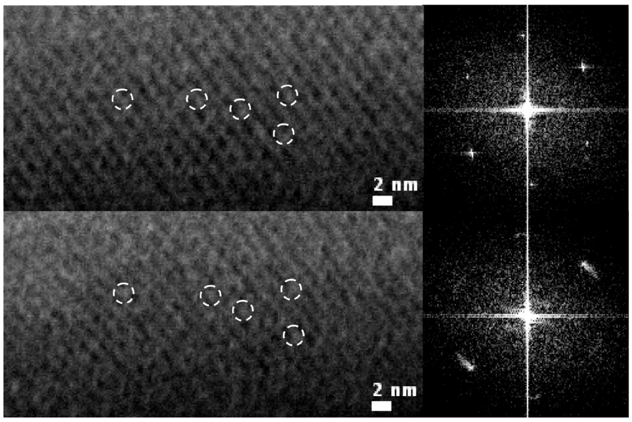

Figure 5. Image of zeolite-supported Ir_6 clusters showing effects of beam damage; the initial (top) and final (bottom) STEM images were recorded for the same region of the sample with an interval of 20 s; the corresponding fast Fourier transforms (FFTs) are shown on the right. The images show that the crystallinity of the zeolite was being destroyed by the beam (note the change in the FFT), but the images do not indicate any aggregation or fragmentation of the iridium clusters.

significant movement of the iridium clusters, some of which are circled in white on the images for identification.

To further investigate the influence of the zeolite framework on the stability of the iridium clusters, we examined an image of the same region shown in Figure 4A taken after 10 s of beam exposure (Figure 6). A comparison of Figure 4A with Figure 6 shows that even after such a short exposure, beam damage of the zeolite framework had already begun. As shown in Figure 6, the beam damage did not occur uniformly across the region shown—the zones inside the yellow ovals experienced much more damage than the others. The clusters (encircled in white in Figure 6) remained intact in the regions where the zeolite framework remained almost unchanged, whereas significant aggregation of the clusters occurred in the regions where zeolite framework had been completely destroyed (denoted by yellow boundaries).

In summary, the images shown in Figure 5 and Figure 6 demonstrate that the zeolite support was highly sensitive to the electron beam. The Ir_6 clusters in the zeolite supercages were quite stable when the zeolite framework was undamaged, but they aggregated quickly once the framework had deteriorated. We attribute the stability of the supported clusters to the isolation and encapsulation by the supercages, and we recognize that there is much more to be learned about the degradation process.

■ EFFECT OF CRYSTALLINITY OF SUPPORT AND SYNTHESIS ROUTE ON UNIFORMITY OF ZEOLITE NaY-SUPPORTED Ir_6 CLUSTERS

In the synthesis of supported metal catalysts, dealuminated zeolites are often preferred over other zeolites as supports to enhance the site isolation of the metal species and to increase thermal stability. However, it has been shown that extensive mesopore formation may take place during zeolite dealumination,[27,28] and as a result amorphous material is formed in the zeolite. The metal species in the dealuminated zeolite could reside inside the mesopores and in amorphous regions and not entirely within the crystalline micropores, which would diminish the uniformity of the anchored metal species.

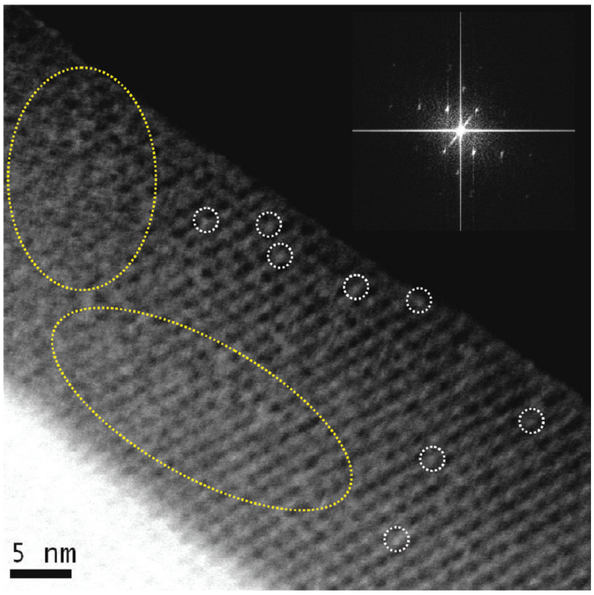

Figure 6. Image of the region shown in Figure 4A, taken after exposure of the sample to the electron beam for 10 s. The clusters encircled in white were in regions where almost no beam damage had occurred, and they did not undergo significant aggregation. In the areas bounded by yellow lines, severe beam damage had occurred, which caused significant aggregation of the iridium clusters.

Therefore, we chose a nondealuminated zeolite as a support with the goal of synthesizing a sample having much higher degree of crystallinity and uniformity than the USY zeolite used in the aforementioned investigation.[29] On the other hand, as a consequence of choosing a zeolite with a high Al content in the framework, as we did (Si/Al atomic ratio = 2.5), imaging was even more challenging than that of the dealuminated Y zeolite sample (Si/Al atomic ratio = 30)[11]—because the zeolite framework stability decreases markedly as the Al content increases.[30,31] Only with quick image acquisition were we able to characterize undamaged samples.

Our sample is nearly ideal for characterization of isolated, monodisperse nanoclusters. We attribute the high degree of uniformity of the sample to the following: (a) the use of a molecular (organometallic) precursor as the starting material for the cluster synthesis—it incorporates only reactive ligands that are easily removed or exchanged and metal atoms that can form stable clusters consisting of only a few atoms, and (b) the use of a highly crystalline porous support, a zeolite, which provides almost identical bonding/nucleation sites for the formation of the nanoclusters and cages for encapsulating them.

■ CATALYTIC ACTIVITY OF CLUSTERS FOR ETHENE HYDROGENATION

The supported iridium clusters were tested for the hydrogenation of ethene. Both the sample incorporating hexairidium carbonyl clusters and that incorporating the decarbonylated clusters were tested as catalysts in a differential tubular plug-flow reactor operated at 298 K and atmospheric pressure. The feed C_2H_4:H_2 molar ratio was 1:2, and the conversions of ethene were kept differential (<5%) to determine catalytic reaction rates directly. The carbonylated sample was found to be catalytically inactive, as expected, because the CO ligands are strongly bound poisons that block

Table 2. Catalytic Activity of Supported Iridium Clusters

catalyst	support	TOF (s^{-1})	reaction conditions	ref.
Ir_2	zeolite NaY	0.029	*a*	20
Ir_4	zeolite NaY	0.043	*a*	20
Ir_6	zeolite NaY	0.032	*a*	20
Ir_6	zeolite NaY	0.26	*b*	this work
Ir_4	MgO	0.052	*c*	34
Ir_6	MgO	0.015	*c*	35
Ir_4	γ-Al_2O_3	0.23	*c*	34
Ir_6	γ-Al_2O_3	0.05	*c*	36

[a] 298 K (P_{hydrogen} = 155 Torr, P_{ethene} = 155 Torr, P_{helium} = 450 Torr). [b] 298 K (P_{hydrogen} = 507 Torr, P_{ethene} = 253 Torr). [c] 295 K (P_{hydrogen} = 100 Torr, P_{ethene} = 40 Torr, P_{helium} = 617 Torr).

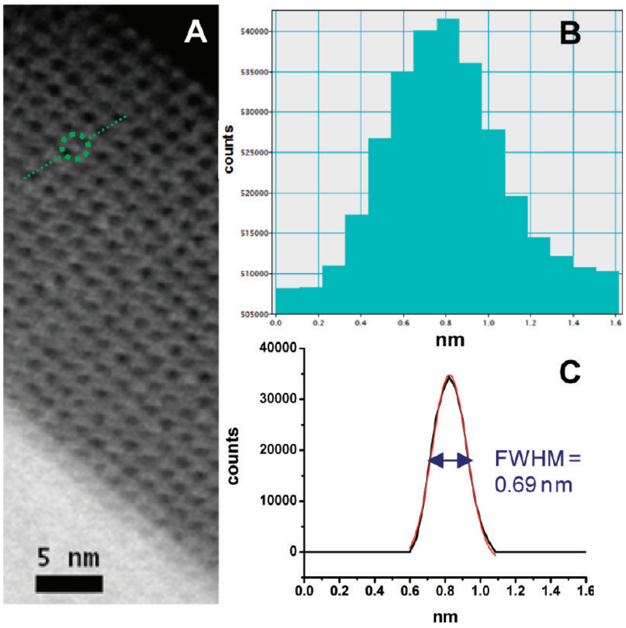

Figure 7. (A) An example cluster encircled in green and line drawn across the cluster for generation of an intensity profile on the HAADF-STEM image of the sample incorporating decarbonylated hexairidium clusters in Figure 4A. (B) Intensity line profile created by Digital Micrograph (Gatan) on the example cluster. (C) Background-subtracted line profile (black), Gaussian fit (red) for the example cluster (OriginPro). Full-width-half-maximum value reported as diameter of cluster metal framework.

access of the reactants to the metal sites.[32] On the other hand, the decarbonylated iridium clusters were catalytically active, characterized by an initial rate of the catalytic reaction (represented by a turnover frequency, TOF) of 0.26 s^{-1}. The only observed product was ethane. This activity is similar to those reported earlier for ethene hydrogenation on small oxide- and zeolite-supported iridium clusters without CO ligands (Table 2).[20,33−36]

CONCLUSIONS

We report the first example of high-dose imaging of uniform hexairidium clusters in the supercages of zeolite NaY. The images were obtained with aberration-corrected high-angle annular dark-field STEM. The images are characterized by a high signal-to-noise ratio, which allowed not only precise measurements of the cluster diameters (0.68 ± 0.14 nm) but also directly locating the clusters in the cages without any image processing. Analysis of 85 clusters showed that 25% were present at T5 sites and 75% at T6 sites.

EXPERIMENTAL METHODS

Synthesis and Sample Handling. Zeolite-supported mononuclear iridium complexes were prepared as before, with the samples handled with standard Schlenk line, glovebox, and glovebag techniques to exclude moisture and air. The zeolite NaY powder (Zeolyst International, CBV100, Si/Al: 2.5 (atomic)) was calcined by heating in flowing O_2 (Airgas, 99.2%) in a once-through reactor as the temperature was ramped at a rate of 3 °C/min from room temperature to 723 K followed by a 4-h soak period at 723 K. Then O_2 flow was stopped and the reactor was evacuated for 16 h at 723 K. The sample was isolated and stored in a glovebox (MBraun) filled with ultrahigh purity argon (Airgas) with a moisture level of 0.5 ppm and an oxygen level less than 5 ppm. Prior to synthesis, *n*-pentane (Fisher Scientific, HPLC grade) was purified in chromatographic columns containing activated Al_2O_3 and activated Al_2O_3-supported copper in a Grubbs apparatus (MBraun) and deoxygenated by sparging with argon (Airgas, UHP, grade 5.0). To prepare the supported iridium complex, $Ir(CO)_2(acac)$ (Strem, 98%), mixed with the calcined zeolite in a Schlenk flask, was slurried in dried *n*-pentane at 298 K for 1 day. The solvent was then removed by evacuation for 1 day. The resultant powder, light yellow in color, was stored in the glovebox.

To form clusters in the zeolite, a ship-in-a-bottle synthesis was carried out with the aforementioned sample in a tubular plug flow reactor treated with 10% CO in helium at 448 K for 16 h; the resulting powder was dark yellow. To form decarbonylated clusters, the latter sample was treated in flowing helium at 573 K for 6 h; the sample turned black.

The treatment gases CO (Matheson, 99.999%) and helium (Airgas, 99.999%) had been purified by passage through traps containing particles of activated γ-Al_2O_3 and of zeolite 4A to remove any traces of metal carbonyls from the high-pressure gas cylinders and moisture, and by traps containing particles of reduced Cu/Al_2O_3 and activated zeolite 4A to remove traces of O_2 and moisture, respectively.

Sample Handling for STEM Experiments. To protect the air-sensitive samples from exposure to the atmosphere, they were prepared by using a lacey carbon, 300-mesh copper grid (Ted-Pella) that was dipped into the powder sample in the argon-filled glovebox (mentioned above) with a moisture level less than 0.5 ppm and an oxygen level less than 5 ppm. After the excess powder was shaken off of the grid, the grid was packed in an Eppendorf tube and sealed with Parafilm inside the glovebox. The tubes under an argon atmosphere in the glovebox were then placed into stainless-steel Swagelok vacuum tubes and sealed with O-rings for air exclusion during the transfer to the microscope facility. In the microscope facility, an argon-filled glovebag (Glas-Col) was set up and purged 5 times with ultrahigh-purity argon (Praxair, grade 5.0). The TEM grid was loaded onto the microscope under the blanket of flowing argon in the glovebag. The glovebag was opened briefly, and the holder was inserted into the microscope and the pumping to evacuate the microscope chamber was initiated within 5 s.

STEM Imaging. Images of the samples were obtained with a JEOL JEM-2100F electron microscope at the University of California, Davis. The microscope is equipped with an FEG, operated at

200 kV, with a CEOS hexapole probe (STEM) aberration corrector, having a probe size of 0.27 nm at full-width-half-maximum (FWHM). The images were captured by an HAADF detector with a collection semiangle of 75−200 mrad and a probe convergence semiangle of 17.1 mrad.

Prior to imaging of the sample, the aberration corrector was aligned with a Pt/Ir on holey carbon standard sample (SPI supplies) until atomic resolution of the metal particles was achieved and lattice spacings of the metals in the standard sample were confirmed.

During imaging of the sample, fast Fourier transforms of the sample were simultaneously monitored to determine the optimal region of imaging.

Cluster Diameter Measurements with HAADF-STEM Images. A total of 85 clusters were analyzed for size measurement in the HAADF-STEM image shown in Figure 4A. For each cluster, an intensity profile was obtained by using the Digital Micrograph software (Gatan). Line profiles were then transferred to OriginPro for baseline correction. Background-subtracted profiles of the clusters were fitted to a Gaussian distribution function in OriginPro, and FWHM values of the fitted peak were reported as the diameter of each cluster metal framework.

Average cluster diameter is reported with a standard deviation for the population of clusters analyzed. Examples of the steps in cluster diameter measurement are depicted in Figure 7 for the HAADF-STEM image of decarbonylated hexairidium clusters in Figure 4A.

ASSOCIATED CONTENT

Ⓢ **Supporting Information.** IR spectra, EXAFS data fitting, and further details of the experimental methods. This material is available free of charge via the Internet at http://pubs.acs.org.

AUTHOR INFORMATION

Corresponding Author

*E-mail: bcgates@ucdavis.edu.

Funding Sources

This work was supported by the Department of Energy (DOE), Grant No. DE-SC0005822 (J.L.) and Grant No. DE-FG02-03ER46057 (C.A.), and the University of California Lab Fee Program. Use of the National Synchrotron Light Source, Brookhaven National Laboratory, was supported by the U.S. Department of Energy, Office of Science, Office of Basic Energy Sciences, under Contract No. DE-AC02-98CH10886.

ACKNOWLEDGMENT

We thank C.-Y. Chen of Chevron for helpful comments. We acknowledge beam time and support of the DOE Office of Science, Materials Sciences, for its role in the operation and development of beam line X-18B at the National Synchrotron Light Source.

REFERENCES

(1) Guzman, J.; Gates, B. C. *Dalton Trans.* **2003**, 3303–3318.

(2) Xu, Z.; Xiao, F.-S.; Purnell, S. K.; Alexeev, O.; Kawi, S.; Deutsch, S. E.; Gates, B. C. *Nature* **1994**, *372*, 346–348.

(3) Fierro-Gonzales, J. C.; Kuba, S.; Hao, Y.; Gates, B. C. *J. Phys. Chem. B* **2006**, *110*, 13326–13351.

(4) Lamb, H. H.; Fung, A. S.; Tooley, P. A.; Puga, J.; Krause, T. R.; Kelley, M. J.; Gates, B. C. *J. Am. Chem. Soc.* **1989**, *111*, 8367–8373.

(5) Gelin, P.; Lefebvre, F.; Elleuch, B.; Naccache, C.; Ben Taarit, Y. In *Intrazeolite Chemistry*; Stucky, G. D., Dwyer, F. G., Eds.; ACS Symposium Series 218; American Chemical Society: Washington, DC, 1983; p 455.

(6) Choi, M.; Wu, Z.; Iglesia, E. *J. Am. Chem. Soc.* **2010**, *132*, 9129–9137.

(7) Ward, E. P. W.; Arslan, I.; Midgley, P. A.; Bleloch, A.; Thomas, J. M. *Chem. Commun.* **2005**, 5805–5807.

(8) Kulkarni, A.; Chi, M.; Ortalan, V.; Browning, N. D.; Gates, B. C. *Angew. Chem., Int. Ed.* **2010**, *49*, 10089–10092.

(9) Ortalan, V.; Uzun, A.; Gates, B. C.; Browning, N. D. *Nat. Nanotechnol.* **2010**, *5*, 843–847.

(10) Kulkarni, A.; J. Lobo-Lapidus, R. J.; Gates, B. C. *Chem. Commun.* **2010**, *46*, 5997–6015.

(11) Ortalan, V.; Uzun, A.; Gates, B. C.; Browning, N. D. *Nat. Nanotechnol.* **2010**, *5*, 506–510.

(12) Li, F.; Gates, B. C. *J. Phys. Chem. B* **2004**, *108*, 11259–11264.

(13) Gates, B. C.; Lamb, H. H. *J. Mol. Catal.* **1989**, *52*, 1–18.

(14) Gates, B. C. *J. Mol. Catal. A: Chem.* **2000**, *163*, 55–65.

(15) Breck, D. W. In *Zeolite Molecular Sieves: Structure, Chemistry, and Use*; Wiley: New York, 1973; pp 29−133.

(16) Fierro-Gonzalez, J. C.; Hao, Y.; Gates, B. C. *J. Phys. Chem. C* **2007**, *111*, 6645–6651.

(17) Garlaschelli, L.; Martinengo, S.; Bellon, P. L.; Demartin, F.; Manassero, M.; Chiang, M. Y.; Wei, C.-Y.; Bau, R. *J. Am. Chem. Soc.* **1984**, *106*, 6664–6667.

(18) Kawi, S.; Gates, B. C. Clusters in Cages. In *Clusters and Colloids: From Theory to Applications*; Schmid, G., Ed.; VCH: New York, 1994; pp 299−365.

(19) Beutel, T.; Kawi, S.; Purnell, S. K.; Knözinger, H.; Gates, B. C. *J. Phys. Chem.* **1993**, *97*, 7284–7289.

(20) Li, F.; Gates, B. C. *J. Phys. Chem. C* **2007**, *111*, 262–267.

(21) Li, F.; Yu, P.; Hartl, M.; Daemen, L. L.; Eckert, J.; Gates, B. C. *Z. Phys. Chem.* **2006**, *220*, 1553–1568.

(22) Tesche, B.; Kawi, S.; Gates, B. C. *Catal. Lett.* **2000**, *70*, 57–60.

(23) Breitscheidel, B.; Zieder, J.; Schubert, U. *Chem. Mater.* **1991**, *3*, 559–566.

(24) Narayan, R.; El-Sayed, M. A. *J. Phys. Chem. B* **2004**, *108*, 8572–8580.

(25) Okamoto, N. L.; Reed, B. W.; Mehraeen, S.; Kulkarni, A.; Morgan, D. G.; Gates, B. C.; Browning, N. D. *J. Phys. Chem. C* **2008**, *112*, 1759–1763.

(26) Kulkarni, A.; Mehraeen, S.; Reed, W. B.; Okamoto, N. L.; Browning, N. D.; Gates, B. C. *J. Phys. Chem. C* **2009**, *113*, 13377–13385.

(27) Janssen, A. H.; Koster, A. J.; de Jong, K. P. *Angew. Chem., Int. Ed.* **2001**, *40*, 1102–1104.

(28) Van Donk, S.; Janssen, A. H.; Bitter, J. H.; de Jong, K. P. *Catal. Rev.* **2003**, *45*, 297–319.

(29) de Jong, K. P.; Zečević, J.; Friedrich, H.; de Jongh, P. E.; Bulut, M.; van Donk, S.; Kenmogne, R.; Finiels, A.; Hulea, V.; Fajula, F. *Angew. Chem., Int. Ed.* **2010**, *49*, 10074–10078.

(30) Kerr, G. T. *Adv. Chem. Ser.* **1973**, *121*, 219–229.

(31) Miessner, H.; Kosslick, H.; Lohse, U.; Parlitz, B.; Tuan, V.-A. *J. Phys. Chem.* **1993**, *97*, 9741–9748.

(32) Grunes, J.; Zhu, J.; Yang, M.; Somorjai, G. A. *Catal. Lett* . **2003**, *86*, 157–161.

(33) Uzun, A.; Dixon, D. A.; Gates, B. C. *ChemCatChem* **2011**, *3*, 95–107.

(34) Argo, A. M.; Odzak, J. F.; Lai, F. S.; Gates, B. C. *Nature* **2002**, *415*, 623–626.

(35) Argo, A. M.; Gates, B. C. *J. Phys. Chem. B* **2003**, *107*, 5519–5528.

(36) Argo, A. M.; Odzak, J. F.; Gates, B. C. *J. Am. Chem. Soc.* **2003**, *125*, 7107–7115.